One-Pot Preparation of Lithium Compensation Layer, Lithiophilic Layer, and Artificial Solid Electrolyte Interphase for Lean-Lithium Metal Anode

Cheng Li,[§] Yan Li,[§] Yongkun Yu, Chunli Shen, Cheng Zhou, Chenxu Dong, Tianhao Zhao, and Xu Xu*

ACCESS | Metrics & More | Article Recommendations | Supporting Information

ABSTRACT: Lithium metal is an ideal anode for high-energy-density batteries. However, the low Coulomb efficiency and the generation of dendrites pose a significant limitation to its practical application, while the excess lithium in the battery also generates serious safety concerns. Herein, a layer-by-layer optimized multilayer structure integrating an artificial solid electrolyte interphase (LiF) layer, a lithiophilic (Li_xAu alloy) layer, and a lithium compensation layer is reported for a lean-lithium metal battery, where each layer acts synergistically to stabilize the lithium deposition behaviors and enhances the cycling performance of the battery. The optimized anode could effectively induce homogeneous reversible lithium deposition under the synergistic effect of multilayer films and keep the integrity of the morphological structure unbroken during the deposition. The presence of the lithium compensation layer allows the half-cell to have a high initial CE of 158.9%, and the action of the LiF layer and lithiophilic layer maintains an average CE of 98.8% over 160 cycles, which further demonstrates the stability of the structure. As a result, when combined with LiFePO_4 cathode, an initial capacity of 148 mAh g^{-1} and a retention rate of 97.5% over 130 cycles were achieved.

KEYWORDS: lean-lithium metal anode, lithium supplementation, physical vapor deposition, lithium fluoride, artificial SEI, lithiophilic current collector
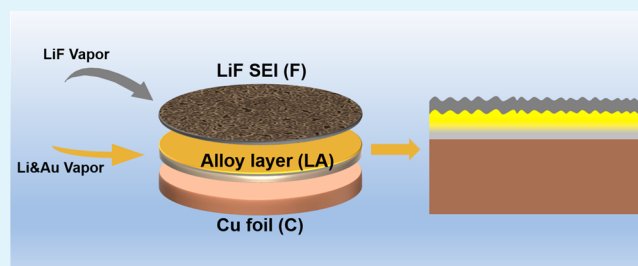
1. INTRODUCTION

The digital energy revolution puts forward higher requirements for the energy density of the next-generation energy storage devices. Replacing the conventional graphite anode with lithium metal can increase the battery energy density by 40–50% because of its high theoretical specific capacity (3860 mAh g^{-1}) and low reduction potential (−3.04 V vs standard hydrogen electrode).[1,2] However, the advantage of these is hidden by the excess lithium metal. The low reduction potential of lithium allows the electrolyte to react irreversibly on its surface to form a solid electrolyte interphase (SEI) layer, and the low Coulomb efficiency (CE) caused by irreversible dead lithium generation during the plating/stripping process has forced the use of excess lithium metal to sacrifice energy density for cycle performance.[3−6] Although there are strategies such as electrolyte additives[7−9] and high specific surface area hosts[10−12] to improve the cycling performance of the lithium metal battery (LMB), the limitation of lithium enrichment is still not well solved. Aiming at the issue of excess anode lithium, in recent years, Qian et al.[13] proposed the concept of an anode-free lithium metal battery (AFLMB), which uses only an ultrathin metal current collector as the anode instead of other active hosts. By directly matching the completely lithiated cathode with the exposed current collector, the anode to cathode capacity ratio can be kept to 1. With this

anode-free structure, the imbalance between energy density and cycling performance in LMB is somewhat moderated, and it has attracted much attention because of its low manufacturing cost and exemplary safety.[14,15]

Although the AFLMB is born out of the LMB, the limiting factors of the LMB are still a significant challenge to the AFLMB. The lithium ions removed from the cathode during the first cycle are limited, and the unstable original SEI layer and the formation of dead lithium greatly accelerate the depletion of the limited lithium sources.[16−18] This is fatal for AFLMB. The challenge of low CE from these unavoidable side effects is magnified in AFLMB, making it an urgent issue. Various lithium compensation strategies[7−9,19−24] have been proposed to alleviate the acute problems caused by the scare lithium source and increase the battery's inclusiveness. The addition of lithium compensation[10,25,26] successfully optimizes the anode-free system to a lean-lithium state. Therefore, the
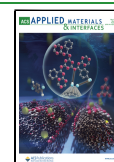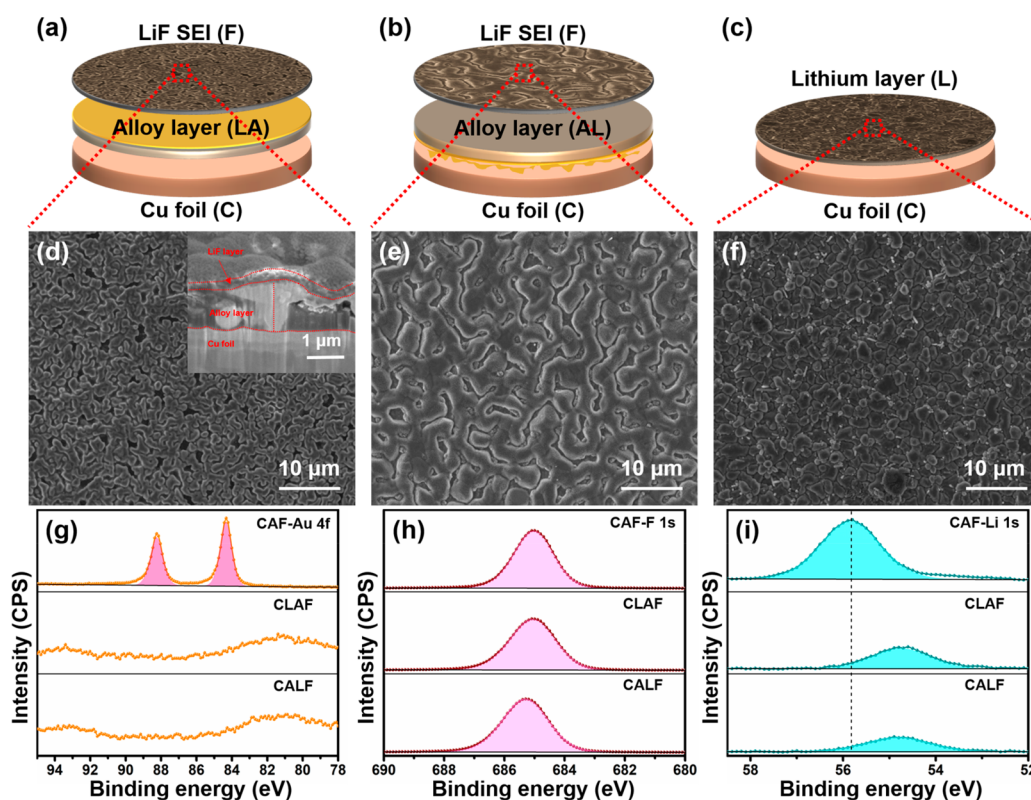
Figure 1. Comparison of the CLAF, CALF, and CL anodes. Schematic diagram of the structure of evaporation anode modification layer: (a) CLAF, (b) CALF, and (c) CL. SEM images of the surface of evaporation anode modification layer (d) CLAF, (e) CALF, and (f) CL. XPS spectra of CLAF, CALF, and CAF: (g) Au 4f, (h) F 1s, and (i) Li 1s.

lean-lithium metal battery (LLMB) has emerged as the times require. The presence of a LLMB is undoubtedly a counterbalance to the limited energy density (mainly in the LMB) and the tight supply of the lithium source (mainly in the AFLMB). The limited lithium supplement significantly alleviates the rapid capacity degradation of the battery at the beginning cycles due to lithium consumption and moderates the energy density limitation caused by excess lithium.[27−30] However, improvement by lithium compensation alone is not enough in the LLMB. The development of the same system also poses similar challenges for the LLMB, and how to further maintain the stability of the electrochemical performances after the exhaustion of the lithium supplement becomes another issue to be addressed.

To improve the performance of the LLMB, we can borrow two main ideas from the LMB strategy. One is to homogenize the nucleation process of lithium in the anode, and the other is to optimize the SEI layer.[31−37] For the nucleation process of lithium, lithiophilic substrates such as Li−Au,[21,38−40] Li−Ag,[24,41] and Li−Zn[42,43] alloys are often used to reduce the nucleation overpotential of lithium and thus achieve homogeneous deposition. Huang et al.[21] used Au-modified Cu foil as a current collector and paired it with a Li_2S cathode to construct AFLMB with a very high energy density up to 626 W kg^{-1}. The Au modification layer will transform to Li_xAu alloy, which can significantly reduce the nucleation barrier of lithium. Moreover, an effective strategy for the growth process is to construct a robust and dense SEI layer with high ionic conductivity, either by optimizing the original SEI layer or constructing an artificial SEI layer to protect the anode from reacting with the electrolyte and to inhibit the growth of

dendrites. Among the various components of the SEI layer, lithium fluoride (LiF)[44−53] has attracted much attention because of its excellent mechanical properties and high surface diffusivity for Li ions. Dahn et al.[8,9] raised the capacity retention of the pouch AFLMB to 80% after 90 cycles by constructing a LiF-rich SEI layer during cycling using the electrolyte of dual-salt LiDFOB/LiBF$_4$. Zhang et al.[45] obtained LiF-protected Cu collectors by the in situ hydrolyzation of lithium hexafluorophosphate (LiPF$_6$), on which bright blue lithium films with uniform columnar shapes were achieved. The hybrid functional films derived by Cui et al.[44] via selective stitching of LiF onto the h-BN interfacial layer using the ALD technique successfully inhibited the formation of Li dendrites and cycled for more than 300 times at high CE. Though these SEI layers obtained by the reactions improve the battery's performance, the controllability of the degree of reaction and the thickness of the SEI layers are still not well resolved.

Inspired by these previous works, we propose the one-pot layer-by-layer preparation using the physical vapor deposition (PVD) technique to optimize the lean-lithium metal anode (LLMA). Direct vapor deposition of the target layer by PVD can regulate the order of the modified layers and precisely control the composition and thickness of each layer. The optimal multilayer structure is obtained by designing different structures for performance comparison, which consists of lithium layer for lithium compensation, Li_xAu alloy as the lithiophilic layer and the LiF as the artificial SEI layer. The synergistic effect of the multilayer structure can successfully control the uniform deposition of lithium and maintain a high average CE of 98.8% after 160 cycles in half-cell. A stable cycle of for 1100 h is achieved in symmetric cells. An initial capacity
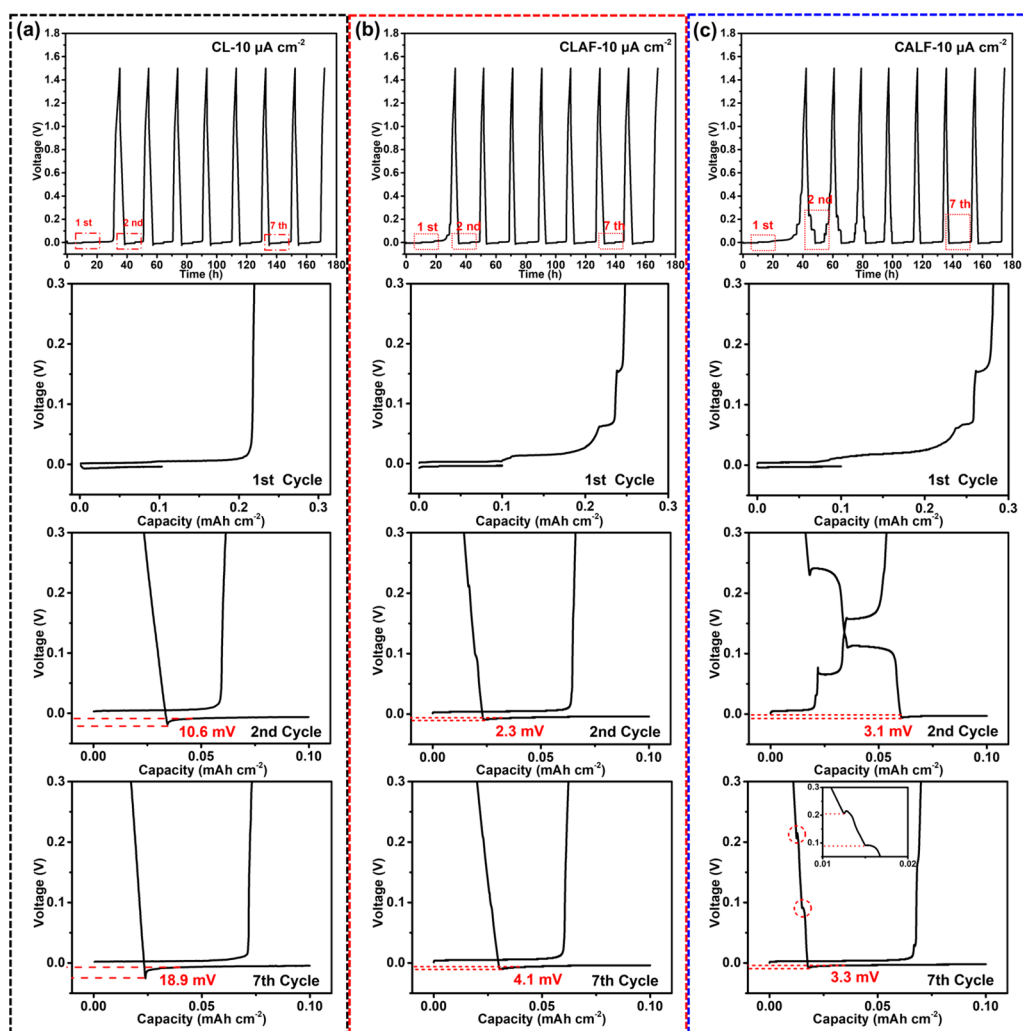
Figure 2. Alloying/dealloying process of a half-cell prepared with a modified anode and Li foil at 10 μA cm^{-2}. Voltage profiles of selected cycles of (a) CL, (b) CLAF, and (c) CALF.

of 148 mAh g^{-1} and 97.5% capacity retention over 130 cycles are also exhibited in the full cell matched with LiFePO$_4$ cathode. It is believed that this work will provide necessary guidance for the optimization of the anodes and provide a new idea for the development of a thin-film battery in the application of microelectronic devices.

2. RESULTS AND DISCUSSION

The two multilayer structures, Cu−Li−Au−LiF (CLAF) and Cu−Au−Li−LiF (CALF), were designed as a comparison according to the different order of lithium and gold evaporation, whereas the only evaporated lithium on copper foil (CL) was designed as a blank control for the LLMA (Figure 1a−c). For comparison, the top view morphology of three different anodes was characterized by SEM (Figure 1d−f). The surfaces of CLAF and CALF show similar texture uniform structure, and that of CLAF is denser. Clear crystal boundaries are shown in pure lithium evaporated CL, but the layer is uneven. The elemental mappings of CLAF and CALF show that the F and Au were uniformly distributed on the surface. At a higher magnification, it is observed that the texture surfaces of the two structures have distinct grains, indicating the existence of LiF (Figure S1). The cross-sectional shear of CLAF using FIB-SEM provides the structural

distribution of the multilayer (inset of Figure 1d). The LiF layer with a uniform thickness of 200 nm tightly covers the surface of the alloy layer and presents an obvious boundary. The LiF layer and the alloy layer form the LA layer as a whole because of the alloying reaction. The XRD tests are performed in a device enclosed with polyimide, to avoid the influence of factors such as water and oxygen in the air on the lithium (Figure S2). In CLAF, CALF, and CL, the peak of Li can be obviously observed (PDF 01-089-7378) in addition to the peak of the Cu substrate and the device. At the same time, there are also obvious peaks of LiF (PDF 01-070-1934) and Li$_{15}$Au$_4$ alloy (Materials Data on Li$_{15}$Au$_4$ (SG:220) by Materials Project) in CLAF and CALF. Because Au exists in the bottom layer of CALF and cannot receive X-ray signals, the bottom side was tested by peeling off the ALF film layer from the Cu foil with polyimide tape. In ALF, in addition to the amorphous peak envelope belonging to polyimide, the obvious existence of Au can also be observed. This indicates that there is Au in CALF that is not involved in the alloying reaction. XPS measurements explored the chemical valence of each layer. The Au 4f spectrum with Au 4f 7/2 at 83.95 eV and Au 5/2 at 87.65 eV can be observed in the structure CAF without lithium, but not in either CLAF or CALF. The spectrum of Li 1s shifts to the right in CLAF at 54.6 eV and CALF at 54.8 eV

compared with CAF at 55.8 eV. The decrease in peak intensity also accompanied it. Only the spectrum of F 1s is kept at 685 eV for all three samples (Figure 1g–i). The results of the XPS show that Li_xAu alloy is formed because of the alloying reaction between Li and Au. The formation of the alloy layer is not the dense film that should be taken for granted, but the formation of regional texture patterns, which also provides sufficient support sites for the LiF artificial SEI layer. Although LiF has good mechanical properties, the dense, flat film layer obtained by direct evaporation of LiF on substrates is prone to stress concentration and fracture.[50,52] Meanwhile, the contact of the LiF layer and Cu substrate is easy to crack apart. This is particularly evident during the plating/stripping of lithium. The evaporation of LiF with a small thickness cannot completely cover the substrate. It will be effective only when the thickness reaches 200 nm (Figure S3). When the Li layer is removed from the structure, uniform deposition of lithium ions can indeed be achieved only under the induction of the Au layer, but the deposition process is accompanied by the alloying reaction resulting in volume expansion (Figure S4 (b)). This volume change is very unfavorable for the LiF layer. In Au@LiF, because of the rigid contact between the film layers, the deposited Li will cause stress concentration in the LiF layer, which eventually leads to a large number of cracks and peelings (Figure S4 (a)). This shows that the Li layer plays an indispensable role in the structure in addition to the effect of lithium supplementation.

To study the alloying process of the three anode materials in the operational condition, we tested half-cell cycles at a low current density (Figure 2). Because there is a small amount of lithium in the anode film, the initial open-circuit voltage in the assembled half-cells is close to 0 V. The cell is discharged at a current density of 10 $\mu A\ cm^{-2}$ to deposit 0.1 mAh cm^{-2} lithium and then charged at the same current to 1.5 V to strip all active lithium from the electrodes. Figure 2a exhibits the voltage−time curves of CL for the first eight cycles and the voltage−capacity curves for the first, second, and seventh cycles. In the first discharge process, CL deposited 0.1 mAh cm^{-2} of lithium but stripped 0.22 mAh cm^{-2} during the charge process, which is due to stripping off the remaining active lithium of the lithium replenishment layer. From this, it can be seen that the lithium replenishment capacity available from CL at 10 $\mu A\ cm^{-2}$ is 0.12 mAh cm^{-2}. Comparing the first cycle of CLAF and CALF in panels b and c in Figure 2, it can be seen that the capacity that their replenishment layers can provide is 0.15 and 0.18 mAh cm^{-2}, respectively. However, all three can provide a lithium replenishment capacity less than the theoretical capacity of the 2 μm Li layer, indicating that reactions consuming the lithium source are occurring on CLAF, CALF, and CL. Combined with the XRD results (Figure S2), it is evident that the alloying reaction occurs during the evaporation of CLAF and CALF and thus consumes part of the lithium source, so that the actual capacity of the Li layer provided is less than that of the 2 μm lithium. CALF has the existence of Au that does not participate in the alloy reaction, so it can provide a higher capacity of lithium replenishment than CLAF. The depletion of the lithium source in CL is mainly attributed to the side reactions that occur when the active lithium is exposed to the electrolyte. This side reaction consumes the lithium source to an even greater level than is required for the alloying process. It also explains the fact that CL has the most active lithium supplement but only provides the least capacity. During the second discharge

process, the lithium ions in CL are directly deposited on the Cu foil exhibiting a larger nucleation overpotential of 10.6 mV, whereas in CLAF and CALF, the lithium ions are deposited on the $Li_{15}Au_4$ with excellent lithophilicity, thus exhibiting only 2.3 and 3.1 mV overpotential, respectively. In CALF, because the first stripping process exposes the bottom Au, all subsequent discharges are accompanied by alloying reactions, corresponding to two voltage plateaus near 0.1 and 0.2 V.[21,39] This alloyed voltage plateau fades out in CALF until the seventh cycle, when CALF also exhibits an overpotential of 3.3 mV. In CLAF, the same lower overpotential of 4.1 mV at the seventh cycle is exhibited because the substrate of the lithium ion is the stable $Li_{15}Au_4$ alloy, whereas in CL, because of the absence of both induction of the lipophilic substrate and protection of the LiF layer, the deposited lithium reacts with the electrolyte in a side reaction to generate a primary SEI layer to repeatedly rupture and repair, thus continuously deteriorating the substrate, showing a large overpotential of 18.9 mV at the seventh cycle.

Compared with CL, the lithium nucleation overpotentials of CLAF and CALF decrease significantly, even closing to 0 V. This is mainly due to the decrease in interface energy caused by lattice matching between lithium and the substrate.[39] Although both Au and Cu have a face-centered cubic structure, which is quite different from the body-centered cubic structure of lithium, Au can react with lithium to form a Li_xAu alloy.[38,39] The surface layer of this solid solution has the same crystal structure as the pure lithium metal, so it can be used as a buffer layer for lithium deposition and effectively eliminate the nucleation barriers. The difference between the curves shown by CLAF and CALF is mainly due to the different evaporation orders. In the evaporation process of the LA layer, Au vapor reacts with lithium, and the lithium is excessive, ensuring that most Au participates in the reaction to form an alloy layer. On the contrary, in the process of AL, Au remains excessive, resulting in an incomplete alloying reaction. Therefore, in the actual deposition process, lithium is deposited on the Li_xAu alloy substrate in CLAF and on the mixed Au and alloy substrate in CALF. The presence of the extra Au causes the lithium to react with the Au during each deposition until all the Au is converted into a stable and irreversible alloy. Although this process can effectively reduce the nucleation overpotential of lithium, it also consumes some of the lithium sources. Furthermore, the conversion of Li_xAu alloys is limited, and multiple alloying/dealloying processes are also accompanied by the volume change of phase transformation, which affects the subsequent cycles.[41] With the increase in current density, when it reaches 0.5 mA cm^{-2}, the advantage of the lithiophilicity of the alloy layer is masked by the large current, but CLAF and CALF still show a minor over potential at 13.9 and 15.2 mV, respectively. CL shows a more enormous overpotential of 33.2 mV as a control. CLAF also presents a small polarization potential of 22.3 mV relative to 31.6 mV of CL, whereas CALF shows a massive potential of 223.5 mV (Figure S5a−c). This is because the bonding between the evaporated AL layer and the substrate is not particularly good, and part of it peels off to increase the internal resistance. This will be more clearly seen in the subsequent micromorphology characterization. The EIS fitting results show that before cycling, CLAF, CALF, and CL exhibit similar initial charge transfer resistance R_{ct} values of 98.5, 104.2, and 115.8 Ω, respectively (Figure S5d). Because of the fact that the primary SEI formed by the reaction between the Li layer and the electrolyte in CL also inhibits the side

reaction after a certain thickness is formed under the static condition, it has the same effect on the charge transfer at the interface as the LiF layer.[54,55] After one cycle of activation, the positive effect of LiF promotes the wetting process between the electrode/electrolyte interface, which improves the charge transfer lowers the R_{ct}. Consequently, CLAF with a stable structure exhibits a low R_{ct} of 14.3 Ω, whereas in CL, the rupture of the primary SEI layer deteriorates the electrode surface, thus causing a certain resistance to charge transfer resulting in an R_{ct} of 56.5 Ω. In CALF, the poor bonding between the ALF layer and the Cu foil also hinders the charge transfer, whereas the cracking of the LiF layer due to stress concentration also eliminates the protective effect, thus exhibiting an R_{ct} of 51.2 Ω similar to that of CL. Meanwhile, we directly charged the assembled half-cells to 1.5 V at 0.5 mA cm^{-2} to completely strip the active lithium source from the electrodes (Figure S6). Because of the alloying reaction during evaporation and the side reaction with the electrolyte, all three can provide less than the theoretical capacity of the 2 μm Li layer in replenishment capacity. The initial lithium replenishment capacities that CL, CLAF, and CALF can provide are 0.09, 0.11, and 0.16 mAh cm^{-2}, respectively.

As mentioned above, the evaporated LiF layer uniformly and tightly covers the textured alloy layer to form LiF domains. The complete coating of LiF on the alloy layer can effectively prevent direct contact between the deposited lithium and the electrolyte. Plating/stripping tests were also carried out in CLA and CAL without evaporated LiF (Figure S7). Under the condition of the current density of 0.5 mA cm^{-2} and areal capacity of 1 mAh cm^{-2}, it can be seen that the surfaces of CLA and CAL have an evident generation of large dendrites, although they are relatively flat under the guide of the alloy layer. The deposited lithium reacts with the electrolyte to form an original SEI layer, and many residues of the original SEI layer can be seen. At the same time, the evaporated coating also has an inevitable fracture. From the side-view SEM, it can be seen that there is a large gap between the AL layer and the substrate of CAL, which indicates that the bond between AL and Cu is unstable (Figure S7f). Without the induction of alloy layer, deposited lithium on CL for 1 mAh cm^{-2} (about 5 μm) shows disordered dendritic deposition, and a large amount of "dead lithium" and original SEI layer remain on the surface after stripping. The side-view SEM images show that the deposited lithium causes a significant fracture to the pre-evaporated lithium layer, which is also one of the factors causing "dead lithium" (Figure 3a−c). After adding a LiF layer on the alloy layer, the situation has been significantly improved. The morphology of CLAF does not change significantly after deposition, showing the same regional texture structure (Figure 3d). After deposition, the macroscopic morphology shows a uniform and dense silver-white deposited lithium (inset in Figure 3d). Benefiting from the protection of the robust LiF layer, there is no trace of the existence of the original SEI layer on the surface of CLAF after stripping. Meanwhile, the whole layer structure is also well maintained (Figure 3e). The deposited lithium of about 5 μm is covered by LiF with the same striations and a relatively flat morphology, which indicates that the lithium ions deposit on the LA layer through the LiF layer and separate the LiF layer from the LA layer (Figure 3f). The lithiophilic LA layer induces a uniform lithium deposition, and the high ionic conductivity of LiF enables the rapid transport of lithium ions across it with a low diffusion energy barrier. The good
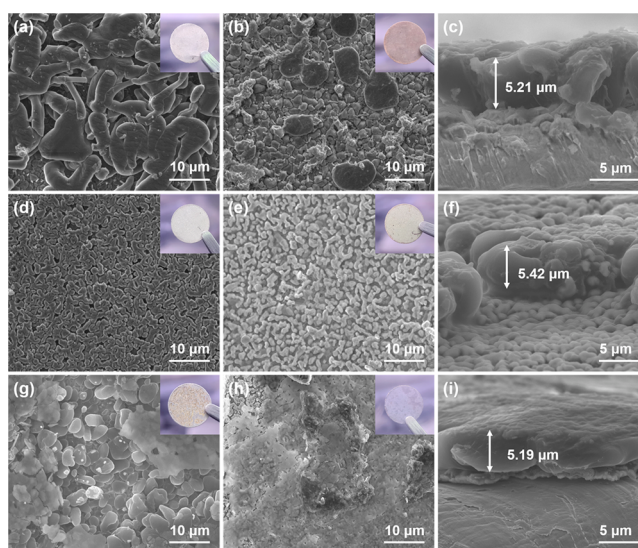

Figure 3. SEM images of lithium deposition behaviors on (a) CL, (d) CLAF, and (g) CALF at 0.5 mA cm^{-2} and 1 mAh cm^{-2}. Lithium stripping behaviors on (b) CL, (e) CLAF, and (h) CALF. Side-view images of lithium deposition on (c) CL, (f) CLAF, and (i) CALF at the same condition.

mechanical property of LiF maintains the stability of the overall structure, isolates the electrolyte, and reduces the generation of the original SEI layer, thereby reducing the unnecessary consumption of lithium sources. The synergy of these multiple effects allows CLAF to maintain the same morphology and structure before and after plating/stripping. The poor binding of the AL layer to the copper substrate results in the rupture of the unfirm layer, making the lithiophilicity of the AL layer inferior to that of the LA layer. The lithium metal on the CALF surface presents a grainlike inhomogeneous deposition, and the stress caused by this huge difference in morphological scale makes the LiF layer overload, resulting in rupture and leaving "dead lithium" after stripping (Figure 3g−i). The current density was kept constant, and the deposited area capacity of lithium was changed to 2 and 3 mAh cm^{-2}, respectively. Comparing the plating/stripping morphology, it is found that the overall structure of CLAF remains intact when the deposition capacity is 2 mAh cm^{-2}. When the capacity reaches 3 mAh cm^{-2}, the structure is partially destroyed, a small amount of the original SEI layer remains, and the film layer is separated from the substrate (Figure S8). This can be explained by the fact that the deposition of excessive volume leads to the rupture of the film layer, and the higher electronic conductivity at the rupture leads to the preferential deposition of lithium ions, which results in a block being located on top of the film layer.

To intuitively compare the growth behavior of dendrites on the designed CLAF and the lean-lithium anode CL, an optical microscope is used for in situ characterization (Figure 4a−d). After 10 min of discharge deposition at a total current of 0.5 mA, the images have shown that CL appears to be dendrite-like lithium deposition and CLAF is a homogeneous layer of lithium deposition (Figure 4c, d). The mechanism of action of these three film layers in the lithium deposition process is summarized in Figure 4e−g. For CLAF, in the first deposition process, lithium ions are driven by potential through the LiF layer to obtain the electrons and are reduced to lithium metal on the LA layer. The LiF and LA layers are separated by the
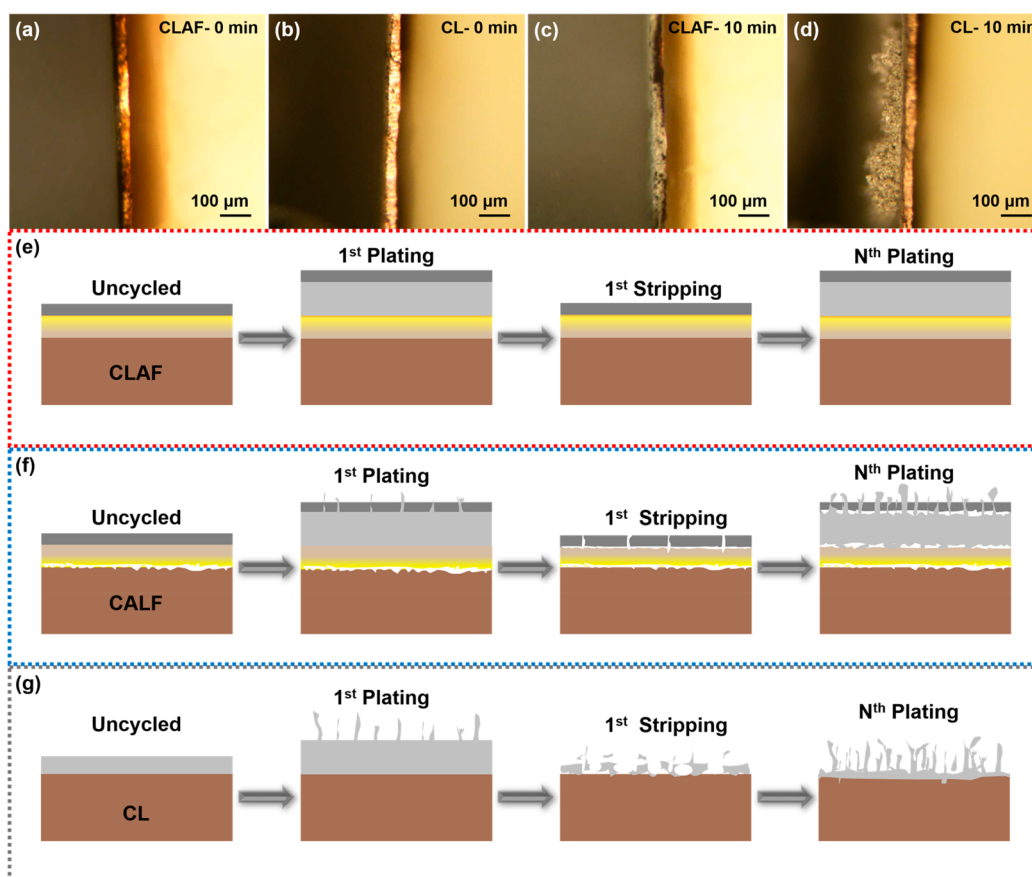
Figure 4. Side view of the optical microscope images on CLAF (a) in the preliminary state and (c) after depositing for 10 min; and CL (b) in the preliminary state and (d) after depositing for 10 min at 0.5 mA. Explanation of the mechanism of lithium deposition and stripping behaviors on (e) CLAF, (f) CALF, and (g) CL.

homogeneous deposited lithium induced by the lithiophilic LA layer. Because lithium deposition is uniform, the LiF layer does not crack. In the subsequent stripping process, the lithium metal between the LA layer and the LiF layer is oxidized to ions and stripped off from the LA layer. At the same time, the lithium compensation layer also begins to play a role. The ALF film retains its structural and functional integrity after stripping. During the following cycle, because of the complete structure and function of the film, lithium plating/stripping can be realized stably and reversibly. In the CLAF structure, the bottom Li layer not only plays the role of lithium replenishment in the cycle, but the soft textured Li also provides good bonding for the subsequent evaporation layers. The middle Au layer reacts to produce $Li_{15}Au_4$ alloy during evaporation to induce the homogeneous deposition of Li ions; at the same time, the gully textured alloy layer also provides sufficient contact sites for the LiF layer, which reduces the rigid constraint of the LiF layer and thus reduces the stress concentration, enabling the uniform and dense cover of LiF. The LiF artificial SEI layer plays the effect of isolating the anode from the electrolyte, avoiding the side reaction between the deposited lithium and the electrolyte, whereas the excellent mechanical properties also inhibit the growth of dendrites. The plating/stripping process of Li ions on CLAF is efficiently and reversibly achieved during long cycling by the synergy of Li layer, Au layer, and LiF layer. The effect of CALF is similar to but not the same as CLAF. Because of the poor contact between the AL layer and Cu substrate, the coverage effect of

the entire ALF film is not as good as that of the LAF film, and some cracks and stress concentration will occur on the surface of the LiF layer. Therefore, in the first deposition process, some of the lithium ions are deposited on the AL layer through the LiF layer, and some of them are directly deposited on the AL layer through the cracks to produce a small number of dendrites. The growth of these dendrites continues to cause the LiF cracks to expand and eventually rupture. When the deposited lithium is stripped off, only the broken LiF layer, part of the "dead lithium," and the original SEI layer are left, and the recovery of the LiF layer and the AL layer is not as good as the original state. After several subsequent deposition cycles, lithium ions are more likely to deposit on the AL layer from the crack of the LiF layer and develop into thick dendrites, which eventually leads to the failure to film. For CL without a protective layer, lithium ions deposit on the pre-evaporated lithium layer randomly to form a large number of dendrites. The pre-evaporated lithium during the stripping process only partially compensates the loss of lithium source caused by the "dead lithium" and the original SEI layer. In the subsequent cycles, the dendrites grow and the lithium source is continuously consumed, which eventually causes the battery to fail. The EDS mappings of the top view and cross sections of CLAF after 10 cycles show that the F elements are uniformly distributed on the surface of the deposited lithium (Figure S9). This indicates that the LiF layer is still well maintained after several cycles. At the same time, the O element distribution is concentrated at the boundary of the film layer, which reflects
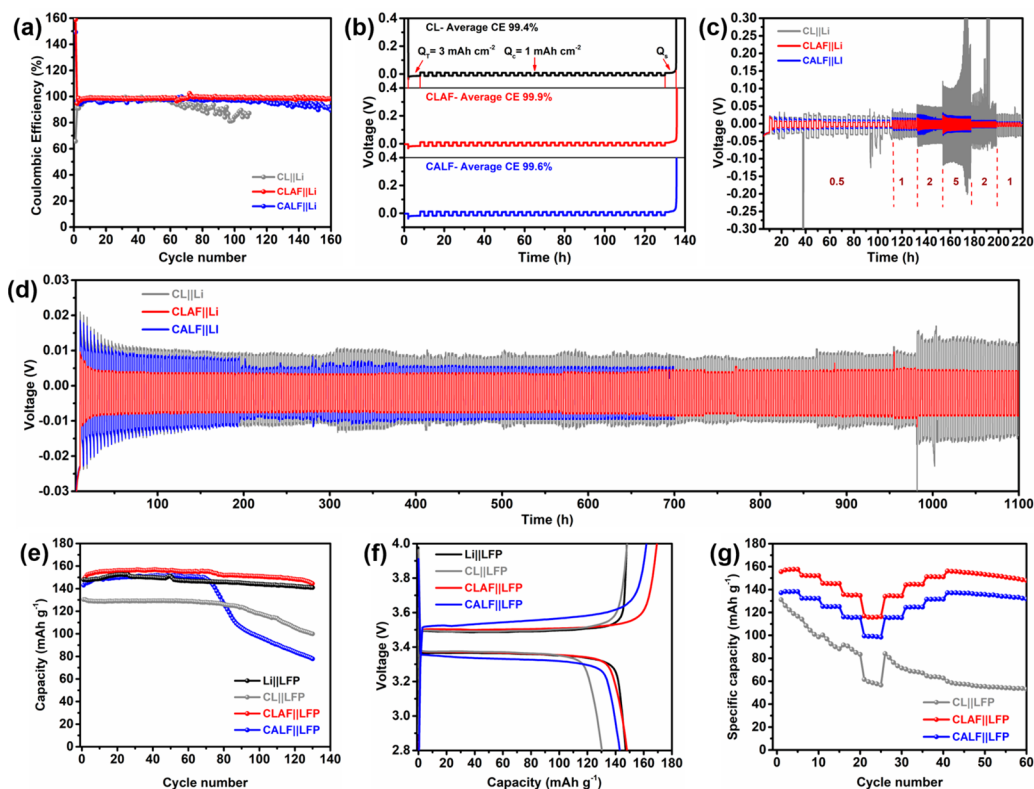
Figure 5. Electrochemical performance: (a) CE of half cells at 0.5 mA cm^{-2} and 1 mAh cm^{-2}, (b) average CE of 30 cycles on symmetrical cells, (c) rate performances of symmetrical cell at 0.5 mA cm^{-2} and 3 mAh cm^{-2} predeposition, and (d) long cycle performances of symmetrical cells at 0.5 mA cm^{-2} and 3 mAh cm^{-2} predeposition. Cycling performances of the full cell prepared with modified anode and LFP: (e) at 0.5 C, (f) charge/discharge voltage plateau in first cycle, and (g) rate performances at 0.2, 0.5, 1, 2, and 5 C.

the deposited Li, whereas the O element distribution is less on its surface, indicating that it is well protected by LiF. In CALF, although a large distribution of F elements can also be found, it can be seen in combination with the morphology that the LiF layer has been massively damaged. The state of the deposited Li can be evaluated by combining the distribution of O elements, and the signal of O elements is stronger in CALF than in CLAF, which indicates that the deposited Li in CALF is exposed without the protection of the LiF layer. The signal of Au is also stronger in CLAF than in CALF, indicating that there is a certain loss of alloying products in CALF after cycling. When the deposition area capacity is increased to 5 mAh/cm^2, the dendrite growth appears on the surfaces of these three kinds of films. However, only the CLAF surface deposits are relatively smooth, and the integrity of the original film layer is maintained better after stripping (Figure S10). Similarly, the CLA and CAL without LiF layer protection show disordered lithium dendrites, leaving many "dead lithium" ions and the original SEI layer after stripping (Figure S11). At the same time, the separation of the AL layer from the Cu substrate is more evident under the action of high-capacity lithium deposition.

The electrochemical performances of the lean-lithium half-cells and full cells employing CLAF, CALF, and CL were comparatively evaluated under various conditions in Figure 5. The three relevant anodes were assembled into half-cells by matching the lithium foil, discharged at a current density of 0.5 mA cm^{-2} and an area capacity of 1 mAh cm^{-2}, and charged to 1.5 V. The CEs of the three anodes are shown in Figure 5a. Under the action of the lithium compensation layer, CLAF demonstrates a high initial CE of 158.9%. It shows a high CE

of 94.8% even in the second cycle after the lithium replenishment effect ends and maintains an average CE of 98.8% after 160 cycles. In contrast, although CALF exhibits a high initial CE of 159.2%, the average CE remains only 96.7%. Moreover, the CE of CALF begin to show obvious attenuation and large fluctuation after 120 cycles. This indicates that CALF begins to collapse, and the plating/stripping process becomes unstable. The CE of the lean-lithium CL, on the other hand, performs unsatisfactorily, with only 65.8% on the first cycle and severe decay after 50 cycles, even with the effect of lithium compensation. The traditional CE test method reflects the reversibility of the whole modified film for lithium plating/stripping. To study the influence of the LiF layer separately, we also adopt a CE test method based on a symmetrical cell (Figure 5b).[56−58] As proposed by Aurbach et al.,[59,60] lithium can be deposited on the substrate first as a lithium reservoir (Q_T), and then the smaller part of the charge (Q_C) can be used to cycle n cycles between the working electrodes and the counter electrodes. After n cycles, the remaining lithium is stripped off completely until the cutoff voltage. The final stripping charge (Q_S) corresponding to the quantity of lithium remaining after cycles is measured. In this test, Q_T = 3 mAh cm^{-2} and Q_C = 1 mAh cm^{-2}, it is worth noting that the lithium replenishment capacity Q_{int} provided by the sample itself also needs to be considered. According to the results in Figure S6, the average CE of CLAF after 30 cycles is as high as 99.7%, whereas the average CEs of CL and CALF are only 98.6 and 99.2%, respectively. This reflects that the LiF layer in CLAF plays a good role in protecting the anode and greatly improves the reversibility of the lithium-ion shuttle. Galvanostatic cycling measurements were also conducted in symmetrical

cells to evaluate the evaporation films' effectiveness. The assembled half-cells discharged an area capacity of 3 mAh cm^{-2} in advance at 0.5 mA cm^{-2} to construct a symmetrical cell. The cells were cycled at a constant current density with a capacity of 1 mA cm^{-2}. In the test of symmetrical cells with different rates (0.5, 1, 2, and 5 mA cm^{-2}), CLAF and CALF show good stability and a small polarization voltage at each rate. Moreover, when it returns to a low current rate, the cells can still cycle stably. The voltage of CL fluctuates at the beginning of the cycle, and it increases suddenly at 5 mA cm^{-2} with a short circuit. When the current returned to 2 mA cm^{-2}, the voltage still shows the short circuit (Figure 5c). In the long cycle experiment of symmetrical cells, CLAF shows a high stability for 1100 h. In contrast, CL presents a higher polarization voltage during the whole test. Because of the premature rupture of the films caused by the poor contact of the AL layer, the CALF cycle is short circuited at about 700 h (Figure 5d). When the operating currents of the symmetric cells are increased to 1 and 3 mA cm^{-2}, respectively, CLAF presents both a smaller polarization voltage and 200 h of stable cycling (Figure S12a, c). In contrast, the CALF∥Li symmetric cell presents a larger voltage relaxation than CLAF before stabilization, and both have a sudden drop in voltage near 90 h of cycling, which reflects a soft short circuit inside the cell (Figure S12b, d). The performance of the symmetric cell reflects the poor stability of the LiF layer on the surface of the CALF electrodes, and the rupture in cycling severely causes the growth of dendrites, which leads to a soft short circuit in the cell. When the designed anode was matched with the LFP cathode to assemble the full cells, it was charged to 4 V and discharged to 2.8 V at 0.5 C. Both CLAF and CALF exhibit an initial discharge capacity equivalent to pure lithium foil (Figure 5e, f). The initial capacities of CLAF, CALF, CL, and lithium foil are 148, 143, 130 and 148 mAh g^{-1}, respectively. After 130 cycles, CLAF shows a capacity retention of 97.5%, even higher than that of lithium foil anode (95.3%), whereas the capacity of CALF begins to decline sharply at about 70 cycles. This explains that CLAF can effectively maintain the reversibility of the cycle in the full cell. Compared with CALF and CL, CLAF has a superior rate performance (Figure 5g). CLAF contributes an initial capacity of 156 mAh g^{-1} at 0.2 C and maintains a reversible capacity of 117 mAh g^{-1} when the current density increases to 5 C. It also provides 152, 145, and 136 mAh g^{-1} at 0.5, 1, and 2 C, respectively, and when it is restored to 0.2 C, it still has a reversible capacity of 156 mAh g^{-1}. The electrochemical performance of the full cells reflects that under the condition of limited lithium, the CLAF anode can provide better capacity retention and maintain more stable lithium plating/stripping behavior. The SEM images of the anode after 10 cycles also show that the CLAF structure is maintained most completely, which reflects the cycling stability of CLAF from another side (Figure S13).

To investigate the growth of the primary SEI layer on the surface of the as-prepared electrodes during cycling, we stripped all the active lithium and performed XPS analysis on the half-cells assembled with the three electrodes after 50 cycles. The composition of the primary SEI layer includes a carbonyl group ($\sim$289.0 eV (CO_3)), polyether carbon ($\sim$286.5 eV (CH_2O)), hydrocarbon ($\sim$284.8 eV (C–C/C–H)), carbonyl carbon ($\sim$288.6 eV), and fluorocarbon ($\sim$292.7 eV) in C 1s spectra, and carbonyl oxygen ($\sim$531.2 eV) and ether oxygen ($\sim$532.7 eV (C–O–C)) in O 1s spectra (Figure S14a, b).[61−63] These common species of carbonaceous and oxygenaceous mainly correspond to the components in the electrolyte. The peaks of all carbonaceous and oxygenaceous species in CLAF and CALF are weaker than CL, which indicates that the protective layer on their surfaces hinders the generation of primary SEI layer. Also, the presence of peaks near 528.2 eV in CL and CALF corresponding to Li_2O in the O 1s pattern is due to the reaction of the electrolyte with the deposited lithium, which is not found in CLAF. This indicates that the deposited lithium does not directly contact with the electrolyte under the synergistic effect of the LAF layer, thus reducing the consumption of the lithium source (Figure S14b). In addition to the peak corresponding to Li_3N near 399.3 eV in the N 1s spectra, peaks corresponding to $LiNO_2$ near 403.9 eV also appear in both CL and CALF, whereas the peak intensity of Li_3N in CLAF is significantly weaker than that of CALF and CL (Figure S14c).[64] It can also be found that the proportion of $ROCO_2Li$ in CL and CALF is much higher than that in CLAF ($\sim$54.6 eV),[65] which is one of the primary SEI components directly obtained by the reaction of ether electrolyte with lithium metal, whereas the largest proportion in CLAF is LiF (Figure S14d). Besides the peaks corresponding mainly to LiF in the F 1s spectra, a large number of fluorocarbon species are present in CL and CALF (Figure S14e). The XPS results on N, Li, and F further demonstrate that the generation of a primary SEI layer was successfully avoided on CLAF because of the synergistic protection of the LAF layer, while the lithium deposited in CL directly reacted with the electrolyte to generate a large amount of primary SEI layer, and at the same time, a certain degree of primary SEI layer also appeared because of the more fragile protective layer of CALF, which was severely damaged during cycling. At the same time, a certain degree of primary SEI layer is also present because the protective layer of CALF is fragile and is severely damaged during cycling. Because of the participation of Au in the alloying reaction, no significant Au 4f signals are detected in CL, CLAF, and CALF (Figure S14f). In the charge/discharge voltage plateau curves at different rates, CLAF presents a smaller polarization voltage than CALF and CL (Figure S15).

3. CONCLUSION

In conclusion, a multilayer consisting of a lithium compensation layer, a lithiophilic layer, and an artificial solid electrolyte interphase was designed and analyzed for the lean-lithium anode. Precise regulation of the structure, composition, and thickness of each layer was achieved by PVD technology and CLAF was proved to be the optimized structure. During cycling, the lithium replenishment, the homogenization nucleation of the lithiophilic LA alloy layer, and the protectively grown lithium of the artificial SEI layer LiF synergize to achieve a great extent of reversibility of lithium in the plating/stripping process. As a result, the CLAF∥Li half-cell achieves a high initial CE of 158.9% and an average CE of 98.8% after 160 cycles with excellent cycle performance, and a stable cycle is achieved for 1100 h in a symmetric cell. Furthermore, in a full cell matched with an LFP cathode, the CLAF anode exhibits an initial capacity of 148 mAh g^{-1} and retention of 97.5%, even higher than that of lithium-metal foil anode (95.3%) after 130 cycles. It is believed that this optimization strategy can be used not only for the lean-lithium metal anode but also for the structural design of other system batteries, which is expected to provide new ideas for the development of thin-film batteries in the application of microelectronic devices.

■ EXPERIMENTAL METHODS

Preparation of the Current-Collector-Modified Layer Structure. The evaporation was performed using a PD-400S physical vapor deposition system (Wuhan PDVACUUM Technologies Co., Ltd., PD-400S). The PVD equipment was equipped with three independent operating boats for the evaporation of Li, Au, and LiF separately. The Cu substrate was previously ultrasonically cleaned with ethanol for 0.5 h and dried in a vacuum oven at 60 °C for 24 h. For the preparation of CLAF, the evaporation of the Li layer was performed at a rate of 20 Å s^{-1} with a thickness of 2 μm. After that, the evaporation of the Au layer was carried out sequentially at a rate of 0.5 Å s^{-1} and a thickness of 80 nm. The evaporation of the LiF layer is executed with a rate of 2 Å s^{-1} and thickness of 200 nm. All the evaporation processes are completed in the same chamber and without vacuum breaking. Adjusting the order of evaporation of Li and Au layers to obtain CALF and CL samples are obtained by evaporating only the Li layer on Cu foil.

Materials Characterization. Structural composition of the as-prepared electrodes was investigated by means of XRD on a MinFlex-600 using Cu K$_\alpha$ radiation. The patterns were recorded between a 10 and 80 °2θ range using a rate of 1° min^{-1}. Scanning electron microscopy (SEM) images were collected using a JEOL JSM-7100F. The chemical states and atomic structure information were investigated by XPS (Thermo-Fisher Scientific-EDCALAB 250Xi).

Electrochemical Measurement. The obtained electrode was assembled into CR2025 coin cells as the cathode in half-cells and symmetrical cells, whereas the anode is commercial Li foil. The full cells were obtained by assembling with the LFP cathode. The LFP cathode was obtained by doctor blading with a loading of 2 mg cm^{-1} and an areal capacity of 0.34 mAh cm^{-2}, and an 8:1:1 LFP:PVDF:NMP slurry. Ether-based electrolyte 1.0 M lithium bis(trilfuoromethanesulfonyl) imide in 1,3-dioxolane (DOL)/dimethyl ether (DME) (v/v = 1:1) with 1% LiNO$_3$ as additive was used for all cells. The amount of liquid electrolyte in all batteries is 60 μL. According to the test of the initial lithium replenishment capacity, the N/P ratios in the CL, CLAF, and CALF full cells are 1.26, 1.32, and 1.47, respectively. The cycle performances were carried out in the Neware CT-4000 multichannel battery test system. The alloying process test was performed on the IVIUM multichannel electrochemical analyzer. An AutoLab PGSTAT302N was used to get electrochemical impedance spectroscopy (EIS) profiles, and the frequency range of the test was set from 0.1 Hz to 1 MHz with an amplitude of 10 mV. In the symmetric cell test, 3 mAh cm^{-2} lithium was predeposited on the electrode in the assembled half-cell. The current density of all batteries during charge—discharge cycles remained at 0.5 mA cm^{-2}. The potential range was between 2.8 and 4.0 V in the full cell test.

■ ASSOCIATED CONTENT

Ⓢ Supporting Information

The Supporting Information is available free of charge at https://pubs.acs.org/doi/10.1021/acsami.2c01716.

> Details for structural and electrochemical performances; elemental mappings of the CLAF and CALF anodes; SEM images of the surface and cross-sectional SEM images of the LiF coating on a copper substrate; SEM images of the surface and cross-sectional SEM images of the lithium plating/stripping behaviors at different conditions on the CLA, CAL, CLAF, CALF, and CL anodes; charge/discharge voltage plateau of the batteries with CLAF, CALF, and CL anodes at different rates (PDF)

■ AUTHOR INFORMATION

Corresponding Author

Xu Xu − *State Key Laboratory of Advanced Technology for Materials Synthesis and Processing, International School of Materials Science and Engineering, Wuhan University of Technology, Wuhan 430070, P. R. China;* ⓘ orcid.org/0000-0002-3309-7596; Email: xuxu@whut.edu.cn

Authors

Cheng Li − *State Key Laboratory of Advanced Technology for Materials Synthesis and Processing, International School of Materials Science and Engineering, Wuhan University of Technology, Wuhan 430070, P. R. China*

Yan Li − *State Key Laboratory of Advanced Technology for Materials Synthesis and Processing, International School of Materials Science and Engineering, Wuhan University of Technology, Wuhan 430070, P. R. China*

Yongkun Yu − *State Key Laboratory of Advanced Technology for Materials Synthesis and Processing, International School of Materials Science and Engineering, Wuhan University of Technology, Wuhan 430070, P. R. China*

Chunli Shen − *State Key Laboratory of Advanced Technology for Materials Synthesis and Processing, International School of Materials Science and Engineering, Wuhan University of Technology, Wuhan 430070, P. R. China*

Cheng Zhou − *State Key Laboratory of Advanced Technology for Materials Synthesis and Processing, International School of Materials Science and Engineering, Wuhan University of Technology, Wuhan 430070, P. R. China*

Chenxu Dong − *State Key Laboratory of Advanced Technology for Materials Synthesis and Processing, International School of Materials Science and Engineering, Wuhan University of Technology, Wuhan 430070, P. R. China*

Tianhao Zhao − *State Key Laboratory of Advanced Technology for Materials Synthesis and Processing, International School of Materials Science and Engineering, Wuhan University of Technology, Wuhan 430070, P. R. China*

Complete contact information is available at:
https://pubs.acs.org/10.1021/acsami.2c01716

Author Contributions

§C. L. and Y. L. contributed equally to this work. The manuscript was written through contributions of all authors. All authors have approval to the final version of the manuscript.

Notes

The authors declare no competing financial interest.

■ ACKNOWLEDGMENTS

■ REFERENCES

(1) Xu, W.; Wang, J.; Ding, F.; Chen, X.; Nasybulin, E.; Zhang, Y.; Zhang, J. G. Lithium Metal Anodes for Rechargeable Batteries. *Energy Environ. Sci.* **2014**, *7* (2), 513−537.

(2) Lin, D.; Liu, Y.; Cui, Y. Reviving the Lithium Metal Anode for High-Energy Batteries. *Nat. Nanotechnol.* **2017**, *12* (3), 194−206.

(3) Ding, J. F.; Xu, R.; Yan, C.; Li, B. Q.; Yuan, H.; Huang, J. Q. A Review on the Failure and Regulation of Solid Electrolyte Interphase in Lithium Batteries. *J. Energy Chem.* **2021**, *59*, 306−319.

(4) Shen, X.; Zhang, X. Q.; Ding, F.; Huang, J. Q.; Xu, R.; Chen, X.; Yan, C.; Su, F. Y.; Chen, C. M.; Liu, X.; Zhang, Q. Advanced Electrode Materials in Lithium Batteries: Retrospect and Prospect. *Energy Mater. Adv.* **2021**, *2021*, 1−15.

(5) Jiang, F.; Yang, S.; Liu, H.; Cheng, X.; Liu, L.; Xiang, R.; Zhang, Q.; Kaskel, S.; Huang, J. Mechanism Understanding for Stripping Electrochemistry of Li Metal Anode. *SusMat* **2021**, *1* (4), 506−536.

(6) Ding, J. F.; Xu, R.; Ma, X. X.; Xiao, Y.; Yao, Y. X.; Yan, C.; Huang, J. Q. Quantification of the Dynamic Interface Evolution in High-Efficiency Working Li-Metal Batteries. *Angew. Chemie. Int. Ed.* **2022**, *61* (13), e202115602.

(7) Beyene, T. T.; Bezabh, H. K.; Weret, M. A.; Hagos, T. M.; Huang, C. J.; Wang, C. H.; Su, W. N.; Dai, H.; Hwang, B. J. Concentrated Dual-Salt Electrolyte to Stabilize Li Metal and Increase Cycle Life of Anode Free Li-Metal Batteries. *J. Electrochem. Soc.* **2019**, *166* (8), A1501−A1509.

(8) Weber, R.; Genovese, M.; Louli, A. J.; Hames, S.; Martin, C.; Hill, I. G.; Dahn, J. R. Long Cycle Life and Dendrite-Free Lithium Morphology in Anode-Free Lithium Pouch Cells Enabled by a Dual-Salt Liquid Electrolyte. *Nat. Energy* **2019**, *4* (8), 683−689.

(9) Louli, A. J.; Eldesoky, A.; Weber, R.; Genovese, M.; Coon, M.; deGooyer, J.; Deng, Z.; White, R. T.; Lee, J.; Rodgers, T.; Petibon, R.; Hy, S.; Cheng, S. J. H.; Dahn, J. R. Diagnosing and Correcting Anode-Free Cell Failure via Electrolyte and Morphological Analysis. *Nat. Energy* **2020**, *5* (9), 693−702.

(10) Chen, H.; Yang, Y.; Boyle, D. T.; Jeong, Y. K.; Xu, R.; de Vasconcelos, L. S.; Huang, Z.; Wang, H.; Wang, H.; Huang, W.; Li, H.; Wang, J.; Gu, H.; Matsumoto, R.; Motohashi, K.; Nakayama, Y.; Zhao, K.; Cui, Y. Free-Standing Ultrathin Lithium Metal-Graphene Oxide Host Foils with Controllable Thickness for Lithium Batteries. *Nat. Energy* **2021**, *6* (8), 790−798.

(11) Huang, W.; Yu, Y.; Hou, Z.; Liang, Z.; Zheng, Y.; Quan, Z.; Lu, Y. C. Dendrite-Free Lithium Electrode Enabled by Graphene Aerogels with Gradient Porosity. *Energy Storage Mater.* **2020**, *33*, 329−335.

(12) Li, Z.; He, Q.; Xu, X.; Zhao, Y.; Liu, X.; Zhou, C.; Ai, D.; Xia, L.; Mai, L. A 3D Nitrogen-Doped Graphene/TiN Nanowires Composite as a Strong Polysulfide Anchor for Lithium-Sulfur Batteries with Enhanced Rate Performance and High Areal Capacity. *Adv. Mater.* **2018**, *30* (45), 1804089.

(13) Qian, J.; Adams, B. D.; Zheng, J.; Xu, W.; Henderson, W. A.; Wang, J.; Bowden, M. E.; Xu, S.; Hu, J.; Zhang, J. G. Anode-Free Rechargeable Lithium Metal Batteries. *Adv. Funct. Mater.* **2016**, *26* (39), 7094−7102.

(14) Nanda, S.; Gupta, A.; Manthiram, A. Anode-Free Full Cells: A Pathway to High-Energy Density Lithium-Metal Batteries. *Adv. Energy Mater.* **2021**, *11* (2), 2000804.

(15) Tian, Y.; An, Y.; Wei, C.; Jiang, H.; Xiong, S.; Feng, J.; Qian, Y. Recently Advances and Perspectives of Anode-Free Rechargeable Batteries. *Nano Energy* **2020**, *78*, 105344.

(16) Xie, Z.; Wu, Z.; An, X.; Yue, X.; Wang, J.; Abudula, A.; Guan, G. Anode-Free Rechargeable Lithium Metal Batteries: Progress and Prospects. *Energy Storage Mater.* **2020**, *32*, 386−401.

(17) Salvatierra, R. V.; Chen, W.; Tour, J. M. What Can Be Expected from ″Anode-Free″ Lithium Metal Batteries? *Adv. Energy Sustain. Res.* **2021**, *2* (5), 2000110.

(18) Hagos, T. M.; Bezabh, H. K.; Huang, C. J.; Jiang, S. K.; Su, W. N.; Hwang, B. J. A Powerful Protocol Based on Anode-Free Cells Combined with Various Analytical Techniques. *Acc. Chem. Res.* **2021**, *54* (24), 4474−4485.

(19) Pande, V.; Viswanathan, V. Computational Screening of Current Collectors for Enabling Anode-Free Lithium Metal Batteries. *ACS Energy Lett.* **2019**, *4* (12), 2952−2959.

(20) Sahalie, N. A.; Wondimkun, Z. T.; Su, W. N.; Weret, M. A.; Fenta, F. W.; Berhe, G. B.; Huang, C. J.; Hsu, Y. C.; Hwang, B. J. Multifunctional Properties of Al_2O_3/Polyacrylonitrile Composite Coating on Cu to Suppress Dendritic Growth in Anode-Free Li-Metal Battery. *ACS Appl. Energy Mater.* **2020**, *3* (8), 7666−7679.

(21) Chen, J.; Xiang, J.; Chen, X.; Yuan, L.; Li, Z.; Huang, Y. Li_2S-Based Anode-Free Full Batteries with Modified Cu Current Collector. *Energy Storage Mater.* **2020**, *30*, 179−186.

(22) Nanda, S.; Bhargav, A.; Manthiram, A. Anode-Free, Lean-Electrolyte Lithium-Sulfur Batteries Enabled by Tellurium-Stabilized Lithium Deposition. *Joule* **2020**, *4* (5), 1121−1135.

(23) Zhang, J.; Chen, H.; Wen, M.; Shen, K.; Chen, Q.; Hou, G.; Tang, Y. Lithiophilic 3D Copper-Based Magnetic Current Collector for Lithium-Free Anode to Realize Deep Lithium Deposition. *Adv. Funct. Mater.* **2022**, *32*, 2110110.

(24) Wondimkun, Z. T.; Tegegne, W. A.; Shi-Kai, J.; Huang, C. J.; Sahalie, N. A.; Weret, M. A.; Hsu, J. Y.; Hsieh, P. L.; Huang, Y. S.; Wu, S. H.; Su, W. N.; Hwang, B. J. Highly-Lithiophilic Ag@PDA-GO Film to Suppress Dendrite Formation on Cu Substrate in Anode-Free Lithium Metal Batteries. *Energy Storage Mater.* **2021**, *35*, 334−344.

(25) Zhang, K.; Qi, J.; Song, J.; Zuo, Y.; Yang, Y.; Yang, T.; Chen, T.; Liu, X.; Chen, L.; Xia, D. Sulfuration of Li-rich Mn-based Cathode Materials for Multi-Anionic Redox and Stabilized Coordination Environment. *Adv. Mater.* **2022**, *34*, 2109564.

(26) Du, J.; Wang, W.; Wan, M.; Wang, X.; Li, G.; Tan, Y.; Li, C.; Tu, S.; Sun, Y. Doctor-Blade Casting Fabrication of Ultrathin Li Metal Electrode for High-Energy-Density Batteries. *Adv. Energy Mater.* **2021**, *11* (45), 2102259.

(27) Lu, K.; Liu, Y.; Chen, J.; Zhang, Z.; Cheng, Y. Redox Catalytic and Quasi-Solid Sulfur Conversion for High-Capacity Lean Lithium Sulfur Batteries. *ACS Nano* **2019**, *13* (12), 14540−14548.

(28) Zhou, J.; Wu, T.; Pan, Y.; Zhu, J.; Chen, X.; Peng, C.; Shu, C.; Kong, L.; Tang, W.; Chou, S. L. Packing Sulfur Species by Phosphorene-Derived Catalytic Interface for Electrolyte-Lean Lithium-Sulfur Batteries. *Adv. Funct. Mater.* **2022**, *32* (4), 2106966.

(29) Kautz, D. J.; Tao, L.; Mu, L.; Nordlund, D.; Feng, X.; Zheng, Z.; Lin, F. Understanding the Critical Chemistry to Inhibit Lithium Consumption in Lean Lithium Metal Composite Anodes. *J. Mater. Chem. A* **2018**, *6* (33), 16003−16011.

(30) Tao, L.; Xu, Z.; Kuai, C.; Zheng, X.; Wall, C. E.; Jiang, C.; Esker, A. R.; Zheng, Z.; Lin, F. Flexible Lignin Carbon Membranes with Surface Ozonolysis to Host Lean Lithium Metal Anodes for Nickel-Rich Layered Oxide Batteries. *Energy Storage Mater.* **2020**, *24*, 129−137.

(31) Chen, X. R.; Zhao, B. C.; Yan, C.; Zhang, Q. Review on Li Deposition in Working Batteries: From Nucleation to Early Growth. *Adv. Mater.* **2021**, *33* (8), 2004128.

(32) Duan, H.; Chen, W.-P.; Fan, M.; Wang, W.-P.; Yu, L.; Tan, S.-J.; Chen, X.; Zhang, Q.; Xin, S.; Wan, L.-J.; Guo, Y.-G. Building an Air Stable and Lithium Deposition Regulable Garnet Interface from Moderate-Temperature Conversion Chemistry. *Angew. Chemie. Int. Ed.* **2020**, *59* (29), 12069−12075.

(33) Jin, T.; Liu, M.; Su, K.; Lu, Y.; Cheng, G.; Liu, Y.; Li, N. W.; Yu, L. Polymer Zwitterion-Based Artificial Interphase Layers for Stable Lithium Metal Anodes. *ACS Appl. Mater. Interfaces* **2021**, *13* (48), 57489−57496.

(34) Li, N. W.; Shi, Y.; Yin, Y. X.; Zeng, X. X.; Li, J. Y.; Li, C. J.; Wan, L. J.; Wen, R.; Guo, Y. G. A Flexible Solid Electrolyte Interphase Layer for Long-Life Lithium Metal Anodes. *Angew. Chemie. Int. Ed.* **2018**, *57* (6), 1505−1509.

(35) Li, N. W.; Yin, Y. X.; Yang, C. P.; Guo, Y. G. An Artificial Solid Electrolyte Interphase Layer for Stable Lithium Metal Anodes. *Adv. Mater.* **2016**, *28* (9), 1853−1858.

(36) Liu, H.; Cheng, X. B.; Huang, J. Q.; Yuan, H.; Lu, Y.; Yan, C.; Zhu, G. L.; Xu, R.; Zhao, C. Z.; Hou, L. P.; He, C.; Kaskel, S.; Zhang,

Q. Controlling Dendrite Growth in Solid-State Electrolytes. *ACS Energy Lett.* **2020**, *5* (3), 833−843.

(37) Um, J. H.; Yu, S. H. Unraveling the Mechanisms of Lithium Metal Plating/Stripping via In Situ/Operando Analytical Techniques. *Adv. Energy Mater.* **2021**, *11* (27), 2003004.

(38) Pelton, A. D. The Au-Li (Gold-Lithium) System. *Bull. Alloy Phase Diagrams* **1986**, *7* (3), 228−231.

(39) Yan, K.; Lu, Z.; Lee, H. W.; Xiong, F.; Hsu, P. C.; Li, Y.; Zhao, J.; Chu, S.; Cui, Y. Selective Deposition and Stable Encapsulation of Lithium through Heterogeneous Seeded Growth. *Nat. Energy* **2016**, *1* (3), 1−8.

(40) Liao, X.; Liu, Q.; Liu, X.; Zhu, S.; Zhao, K.; Zhao, Y. A Facile Surface Alloy-Engineering Route to Enable Robust Lithium Metal Anodes. *Phys. Chem. Chem. Phys.* **2022**, *24* (8), 4751−4758.

(41) Zhang, S.; Yang, G.; Liu, Z.; Weng, S.; Li, X.; Wang, X.; Gao, Y.; Wang, Z.; Chen, L. Phase Diagram Determined Lithium Plating/Stripping Behaviors on Lithiophilic Substrates. *ACS Energy Lett.* **2021**, *6* (11), 4118−4126.

(42) Wang, G.; Xiong, X.; Zou, P.; Fu, X.; Lin, Z.; Li, Y.; Liu, Y.; Yang, C.; Liu, M. Lithiated Zinc Oxide Nanorod Arrays on Copper Current Collectors for Robust Li Metal Anodes. *Chem. Eng. J.* **2019**, *378*, 122243.

(43) Zhao, F.; Zhou, X.; Deng, W.; Liu, Z. Entrapping Lithium Deposition in Lithiophilic Reservoir Constructed by Vertically Aligned ZnO Nanosheets for Dendrite-Free Li Metal Anodes. *Nano Energy* **2019**, *62*, 55−63.

(44) Xie, J.; Liao, L.; Gong, Y.; Li, Y.; Shi, F.; Pei, A.; Sun, J.; Zhang, R.; Kong, B.; Subbaraman, R.; et al. Stitching H-BN by Atomic Layer Deposition of LiF as a Stable Interface for Lithium Metal Anode. *Sci. Adv.* **2017**, *3* (11), eaao3170.

(45) Zhang, X. Q.; Chen, X.; Xu, R.; Cheng, X. B.; Peng, H. J.; Zhang, R.; Huang, J. Q.; Zhang, Q. Columnar Lithium Metal Anodes. *Angew. Chemie. Int. Ed.* **2017**, *129* (45), 14395−14399.

(46) Strmcnik, D.; Castelli, I. E.; Connell, J. G.; Haering, D.; Zorko, M.; Martins, P.; Lopes, P. P.; Genorio, B.; Østergaard, T.; Gasteiger, H. A.; Maglia, F.; Antonopoulos, B. K.; Stamenkovic, V. R.; Rossmeisl, J.; Markovic, N. M. Electrocatalytic Transformation of HF Impurity to H_2 and LiF in Lithium-Ion Batteries. *Nat. Catal.* **2018**, *1* (4), 255−262.

(47) Lang, J.; Long, Y.; Qu, J.; Luo, X.; Wei, H.; Huang, K.; Zhang, H.; Qi, L.; Zhang, Q.; Li, Z.; Wu, H. One-Pot Solution Coating of High Quality LiF Layer to Stabilize Li Metal Anode. *Energy Storage Mater.* **2019**, *16*, 85−90.

(48) Yuan, Y.; Wu, F.; Bai, Y.; Li, Y.; Chen, G.; Wang, Z.; Wu, C. Regulating Li Deposition by Constructing LiF-Rich Host for Dendrite-Free Lithium Metal Anode. *Energy Storage Mater.* **2019**, *16*, 411−418.

(49) Xie, Z.; Wu, Z.; An, X.; Yue, X.; Yoshida, A.; Du, X.; Hao, X.; Abudula, A.; Guan, G. 2-Fluoropyridine: A Novel Electrolyte Additive for Lithium Metal Batteries with High Areal Capacity as Well as High Cycling Stability. *Chem. Eng. J.* **2020**, *393*, 124789.

(50) Tan, J.; Matz, J.; Dong, P.; Shen, J.; Ye, M. A Growing Appreciation for the Role of LiF in the Solid Electrolyte Interphase. *Adv. Energy Mater.* **2021**, *11* (6), 2100046.

(51) Shadike, Z.; Lee, H.; Borodin, O.; Cao, X.; Fan, X.; Wang, X.; Lin, R.; Bak, S. M.; Ghose, S.; Xu, K.; Wang, C.; Liu, J.; Xiao, J.; Yang, X. Q.; Hu, E. Identification of LiH and Nanocrystalline LiF in the Solid-Electrolyte Interphase of Lithium Metal Anodes. *Nat. Nanotechnol.* **2021**, *16* (5), 549−554.

(52) Smeu, M.; Leung, K. Electron Leakage through Heterogeneous LiF on Lithium-Metal Battery Anodes. *Phys. Chem. Chem. Phys.* **2021**, *23* (5), 3214−3218.

(53) Zhang, Q.; Wei, X.; Liu, Y. S.; Liu, X.; Bai, W. L.; Zhang, Z.; Wang, K. X.; Chen, J. S. Dendrite-Free Lithium Anode Achieved under Lean-Electrolyte Condition through the Modification of Separators with F-Functionalized Ti_3C_2 Nanosheets. *J. Energy Chem.* **2022**, *66*, 366−373.

(54) Feng, Y.; Zhang, C.; Li, B.; Xiong, S.; Song, J. Low-Volume-Change, Dendrite-Free Lithium Metal Anodes Enabled by Lithophilic 3D Matrix with LiF-Enriched Surface. *J. Mater. Chem. A* **2019**, *7* (11), 6090−6098.

(55) Zhang, L.; Zhang, K.; Shi, Z.; Zhang, S. LiF as an Artificial SEI Layer to Enhance the High-Temperature Cycle Performance of $Li_4Ti_5O_{12}$. *Langmuir* **2017**, *33* (42), 11164−11169.

(56) Adams, B. D.; Zheng, J.; Ren, X.; Xu, W.; Zhang, J. G. Accurate Determination of Coulombic Efficiency for Lithium Metal Anodes and Lithium Metal Batteries. *Adv. Energy Mater.* **2018**, *8* (7), 1702097.

(57) Rodriguez, R.; Loeffler, K. E.; Edison, R. A.; Stephens, R. M.; Dolocan, A.; Heller, A.; Mullins, C. B. Effect of the Electrolyte on the Cycling Efficiency of Lithium-Limited Cells and Their Morphology Studied Through in Situ Optical Imaging. *ACS Appl. Energy Mater.* **2018**, *1* (11), 5830−5835.

(58) Genovese, M.; Louli, A. J.; Weber, R.; Hames, S.; Dahn, J. R. Measuring the Coulombic Efficiency of Lithium Metal Cycling in Anode-Free Lithium Metal Batteries. *J. Electrochem. Soc.* **2018**, *165* (14), A3321−A3325.

(59) Aurbach, D.; Granot, E. The Study of Electrolyte Solutions Based on Solvents from the "Glyme" Family (Linear Polyethers) for Secondary Li Battery Systems. *Electrochim. Acta* **1997**, *42* (4), 697−718.

(60) Aurbach, D.; Youngman, O.; Dan, P. The Electrochemical Behavior of 1,3-Dioxolane-LiClO$_4$ Solutions-II. Contaminated Solutions. *Electrochim. Acta* **1990**, *35* (3), 639−655.

(61) Zheng, J.; Engelhard, M. H.; Mei, D.; Jiao, S.; Polzin, B. J.; Zhang, J. G.; Xu, W. Electrolyte Additive Enabled Fast Charging and Stable Cycling Lithium Metal Batteries. *Nat. Energy* **2017**, *2* (3), 1−8.

(62) Jiao, S.; Ren, X.; Cao, R.; Engelhard, M. H.; Liu, Y.; Hu, D.; Mei, D.; Zheng, J.; Zhao, W.; Li, Q.; Liu, N.; Adams, B. D.; Ma, C.; Liu, J.; Zhang, J. G.; Xu, W. Stable Cycling of High-Voltage Lithium Metal Batteries in Ether Electrolytes. *Nat. Energy* **2018**, *3* (9), 739−746.

(63) Liu, S.; Xia, X.; Deng, S.; Xie, D.; Yao, Z.; Zhang, L.; Zhang, S.; Wang, X.; Tu, J. In Situ Solid Electrolyte Interphase from Spray Quenching on Molten Li: A New Way to Construct High-Performance Lithium-Metal Anodes. *Adv. Mater.* **2019**, *31* (3), 1806470.

(64) Liu, S.; Ji, X.; Piao, N.; Chen, J.; Eidson, N.; Xu, J.; Wang, P.; Chen, L.; Zhang, J.; Deng, T.; Hou, S.; Jin, T.; Wan, H.; Li, J.; Tu, J.; Wang, C. An Inorganic-Rich Solid Electrolyte Interphase for Advanced Lithium-Metal Batteries in Carbonate Electrolytes. *Angew. Chemie. Int. Ed.* **2021**, *60* (7), 3661−3671.

(65) Fang, C.; Li, J.; Zhang, M.; Zhang, Y.; Yang, F.; Lee, J. Z.; Lee, M. H.; Alvarado, J.; Schroeder, M. A.; Yang, Y.; Lu, B.; Williams, N.; Ceja, M.; Yang, L.; Cai, M.; Gu, J.; Xu, K.; Wang, X.; Meng, Y. S. Quantifying Inactive Lithium in Lithium Metal Batteries. *Nature* **2019**, *572* (7770), 511−515.